

Photogalvanic probing of helical edge channels in 2D HgTe topological insulators

K.-M. Dantscher,¹ D. A. Kozlov,^{2,3} M. T. Scherr,¹ S. Gebert,¹ J. Bärenfänger,¹ M. V. Durnev,⁴ S. A. Tarasenko,⁴ V. V. Bel'kov,⁴ N. N. Mikhailov,² S. A. Dvoretzky,² Z. D. Kvon,^{2,3} D. Weiss,¹ and S. D. Ganichev¹
¹*Terahertz Center, University of Regensburg, 93040 Regensburg, Germany*
²*A. V. Rzhanov Institute of Semiconductor Physics, Novosibirsk 630090, Russia*
³*Novosibirsk State University, Novosibirsk 630090, Russia and*
⁴*Ioffe Institute, 194021 St. Petersburg, Russia*

We report on the observation of a circular photogalvanic current excited by terahertz (THz) laser radiation in helical edge channels of HgTe-based 2D topological insulators (TIs). The direction of the photocurrent reverses by switching the radiation polarization from right-handed to left-handed one and, for fixed photon helicity, is opposite for the opposite edges. The photocurrent is detected in a wide range of gate voltages. With decreasing the Fermi level below the conduction band bottom, the current emerges, reaches a maximum, decreases, changes its sign close to the charge neutrality point (CNP), and again rises. Conductance measured over a $7\ \mu\text{m}$ distance at CNP approaches $2e^2/h$, the value characteristic for ballistic transport in 2D TIs. The data reveal that the photocurrent is caused by photoionization of helical edge electrons to the conduction band. We discuss the microscopic model of this phenomenon and compare calculations with the experimental data.

PACS numbers:

The quantum spin Hall (QSH) effect occurs in two-dimensional topological insulators and rests on the existence of conducting helical edge states while the bulk of the two-dimensional system is insulating [1–4]. In contrast to the quantum Hall effect, the formation of these edge states requires no magnetic field \mathbf{B} : they stem from the band inversion caused by strong spin-orbit interaction and are, due to the absence of \mathbf{B} , topologically protected by time reversal symmetry. Given that the spin-up and spin-down electrons propagate along an edge in the opposite directions, i.e., the spin projection is locked to the \mathbf{k} -vector, the edge channels are helical in nature. The first experimental evidence for the QSH effect was obtained in HgTe quantum wells (QWs) [5] by observing a resistance plateau around $h/(2e^2)$ in the longitudinal resistance of a mesoscopic Hall bar. Here, h is Planck's constant and e is the elementary charge. This observation was further confirmed by non-local experiments both in the ballistic [6] and diffusive [7] transport regime. Conducting edge channels were later probed by scanning squid microscopy [8], scanning gate microscopy [9], microwave impedance microscopy [10], and by analyzing the spatial distribution of super-currents [11]. The spin polarization of the edge states was investigated so far by electrical means only: by detecting the spin to charge conversion in devices utilizing the inverse spin Hall effect [12] or with ferromagnetic contacts [13].

Here, we use circularly polarized THz radiation to excite selectively spin-up and spin-down electrons circling clockwise and counter-clockwise around the sample edges. We show that the selective excitation causes an imbalance in the electron distribution between positive and negative wave vectors. This is probed as the associated photocurrent, which reverses its direction upon switching the helicity of the radiation polarization.

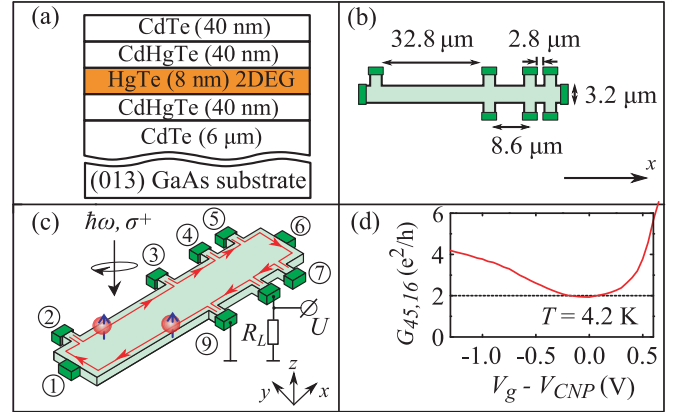


FIG. 1: Cross section (a) and geometry (b) of the studied structures. (c) Experimental setup of the photocurrent measurement. Arrows along edges illustrate spin polarized current excited by circularly polarized radiation. (d) Conductance measured for sample # 1, showing ballistic transport in the vicinity of CNP.

The experiments have been carried out on high-mobility $\text{Hg}_{0.3}\text{Cd}_{0.7}\text{Te}/\text{HgTe}/\text{Hg}_{0.3}\text{Cd}_{0.7}\text{Te}$ single QW structures with a well width $L_w = 8$ nm, having the inverted band ordering [4, 5]. The structures were grown by molecular beam epitaxy on (013)-oriented GaAs substrates [14, 15], the corresponding layer sequence is shown in Fig. 1(a). Several samples have been prepared from the same wafer. The typical Hall bar design, dimensions, and the ohmic contacts positions on the device are shown in Figs. 1(b) and (c). This geometry allows us to study both, magneto-transport and photocurrents induced by THz radiation along the circumference of a sample.

The devices have been patterned by means of photolithography and reactive ion inductively coupled plasma

etching with hydrogen. In order to vary the Fermi level position the devices are equipped with semitransparent Ti(15 nm)/Au(5 nm) gates on top of a 200 nm SiO₂ layer grown by chemical vapour deposition. All samples have been characterized by transport measurements with currents in the range of 10 – 100 nA. The mobility measured at $T = 4.2$ K is about 10^5 cm²/(Vs) at the QW carrier density of $3 \cdot 10^{11}$ cm⁻² at zero gate voltage.

Figure 1(d) shows the 4-terminal conductance at 4.2 K measured for the voltage drop between the contacts 4 and 5 and the current flowing between the contacts 1 and 6. It demonstrates the conductance quantization close to $2e^2/h$, i.e., the system is tuned into the QSH regime. The conductance around $2e^2/h$ is only detected for the closest contact pairs 4-5 and 7-8 (the contact spacing is $2.8 \mu\text{m}$ and the edge length is about $7 \mu\text{m}$). For contact pairs with larger separation, e.g. for the contact pair 3-4, the conductance ranges between $2e^2/h$ and e^2/h . For different sample cool-downs, the CNP can occur at different gate voltages. This is caused by the to cool-down dependent charge trapping in the insulator. While we find the CNP sometimes shifted, the overall behavior of the signals remains unchanged. To compare the measurements taken at different sample cool-downs we plot the data as a function of the normalized gate voltage $V_g - V_{\text{CNP}}$ with V_{CNP} being the gate voltage of CNP.

We excite photocurrents by applying circularly polarized THz radiation of a continuous wave (*cw*) molecular laser [16, 17] under normal incidence. Two radiation frequencies f were chosen: (i) $f = 2.54$ THz with the photon energy $\hbar\omega = 10.4$ meV and (ii) $f = 1.62$ THz with $\hbar\omega = 6.7$ meV. The laser beam with the power $P \approx 10$ mW and an almost Gaussian profile, measured by a pyroelectric camera [18], is focused onto a spot of about 1.5 mm diameter, thus illuminating the whole sample. The radiation intensity $I \approx 0.6$ W/cm² is modulated by an optical chopper at the frequency 600 Hz. To create right-handed (σ^+) and left-handed (σ^-) circularly polarized radiation $\lambda/4$ plates are used. We study the photo-signal generated in the sample by measuring the voltage drop U across a load resistance R_L , see Fig. 1(c), by using two electrical measurement configurations and standard lock-in technique: (i) $R_L = 50 \Omega$ with $R_L \ll R_s$, where R_s is the sample resistance or (ii) $R_L \gg R_s$. In the former case the photocurrent is given by $J = U/R_L$. All experiments are performed at liquid helium temperature.

When illuminating an unbiased devices with circularly polarized radiation we detect a photovoltage U between any pair of contacts along the same edge. The dependence of the photovoltage U_{89} , measured between the contacts 8 and 9 at one edge of the sample, on the gate voltage is shown in Fig. 2(a). The central observation is that the polarity of U_{89} changes upon changing the polarization from σ^+ to σ^- . Furthermore, the helicity dependent signals defined as $U^c = [U(\sigma^+) - U(\sigma^-)]/2$, plotted in Fig. 2(b), show consistently different polarity for con-

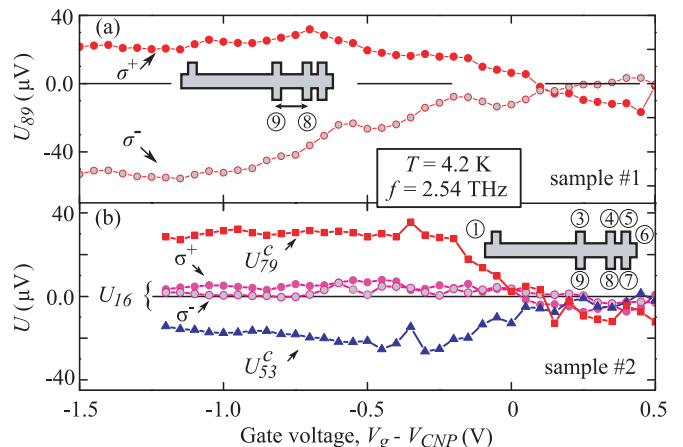


FIG. 2: (a) Photovoltage excited by right-handed (σ^+ , full circles) and left-handed (σ^- , open circles) circularly polarized radiation and measured between contacts 8 and 9 (see inset) as a function of the gate voltage. (b) Photon helicity sensitive photoresponse, $U^c = [U(\sigma^+) - U(\sigma^-)]/2$, obtained for sample #2 for two opposite edges as a function of gate voltage. Full and open circles show the photoresponse U_{16} excited by σ^+ and σ^- radiation and measured over the whole sample.

tacts pairs on the opposite sides of the sample. This indicates that the photoresponse stems from a photocurrent flowing along the edges of the sample. The sense of circulation of the photocurrent depends on the photon helicity. Measurement of U_{16} across the sample, between the contacts 1 and 6, shown in Fig. 2(b), confirms this scenario: the signals are vanishingly small, which is ascribed to the compensation of the counter propagating currents generated along the opposite edges. Interestingly, the signs of the voltages caused by the *edge* photosignal reverse at the gate voltage between 0 and 0.5 V heralding that the sense of circulation of the edge current changes as a function of the gate voltage, see Fig. 2(b).

The measured circular photocurrent $J_x^c = [J(\sigma^+) - J(\sigma^-)]/2$, obtained for $R_L \ll R_s$, is displayed in Figs. 3(a) and (c) and exhibits similar behavior. The data are shown for two THz frequencies corresponding to $\hbar\omega = 10.4$ meV (panel a) and $\hbar\omega = 6.7$ meV (panel c), i.e., the photon energies smaller than the bulk gap. The fact that *edge* currents at the opposite sides of the sample have, in contrast to *bulk* currents, opposite polarities allows us to refine the edge current contribution J_{edge}^c by subtracting the currents measured at the opposite sides, $J_{\text{edge}}^c = (J_{43}^c - J_{89}^c)/2$. The corresponding data are shown in Figs. 3(b) and (d). By summing up the currents, $J_{\text{QW}}^c = (J_{43}^c + J_{89}^c)/2$, we obtain the bulk contribution which is shown in the inset of Fig. 3(d). Remarkably, the sign of the edge current J_{edge}^c changes twice: at a gate voltage close to the CNP and at $V_g - V_{\text{CNP}} \approx 2$ V, while the bulk contribution J_{QW}^c is noticeable only for larger gate voltages. The central result so far is that we can selectively excite left- and right-moving edge currents by

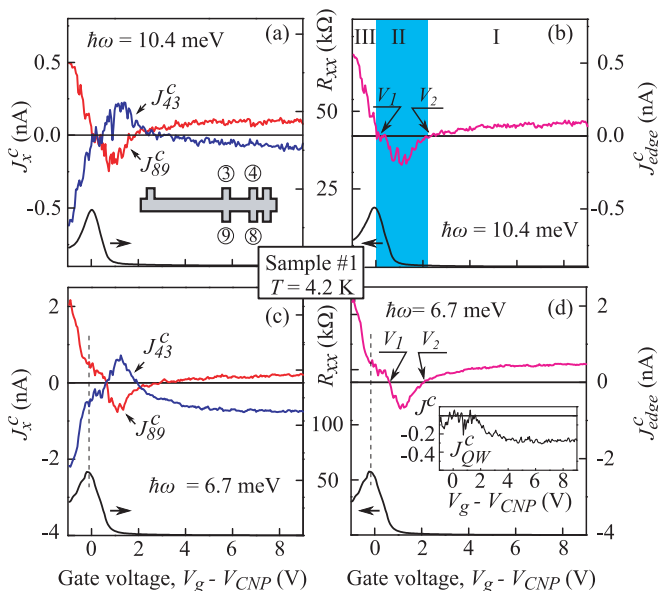


FIG. 3: (a) and (c): Circular photocurrents $J_x^c = [J(\sigma^+) - J(\sigma^-)]/2$ obtained for $R_L \ll R_s$ for two contact pairs at the opposite edges, see inset in panel (a). Black solid curves show the sample resistance measured between the contacts 3 and 4. (b) and (d) Edge and QW bulk (inset) contributions.

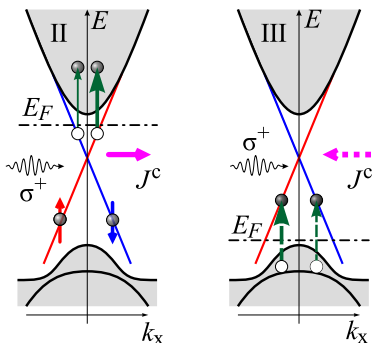


FIG. 4: Schematic picture of optical transitions for right-handed circularly polarized radiation and the photocurrent formation for two positions of the Fermi level E_F in the bulk gap. k_x is the wave vector along the sample edge. Region II: E_F is below the conduction-band bottom E_c and $E_c - E_F < \hbar\omega$. Region III: E_F is close to the valence band top.

means of the helicity of circularly polarized radiation, in accordance with the helical nature of these states. Below we resort to a microscopic model to understand the origin of the photocurrents in the different gate voltage regions, marked by I to III in Fig. 3(b). Region II corresponds to the gate voltages between the nodes of the photocurrent, whereas regions I and III correspond to gate voltages above and below the borders of the region II. Note that the border between region II and III is close to the CNP.

In region I, i.e., at $V_g - V_{CNP} > 2$ V, the Fermi level lies in the conduction band, as it follows from transport measurement, see the resistance R_{xx} in Fig. 3(b). In this

region, both bulk and edge photocurrents are formed by conduction-band carriers. The reduced symmetry at the sample edges results in an asymmetric scattering of carriers causing an edge current with the direction determined by the helicity of the THz field. This mechanism has been explored before in graphene and other 2D materials [19, 20] and is also active here.

If E_F is in the bulk gap the above mechanism is no longer effective and the presence of topological edge states needs to be taken into account to explain the current formation. Figure 4 illustrates the linear dispersion of helical edge states between the schematic valence and conduction band. The branches of the dispersion are spin polarized as marked by arrows in panel (a). The edge states with the positive velocity along x direction are formed mainly from $|E1, +1/2\rangle$ and $|H1, +3/2\rangle$ subbands and have pseudospin $s = +1/2$ (spin-up branch) [21, 22]. Counter propagating electrons have $s = -1/2$ (spin-down branch) and these edge states are mainly formed from $|E1, -1/2\rangle$ and $|H1, -3/2\rangle$ subbands.

The Fermi level crosses the bottom of the conduction band and enters the bulk gap at gate voltage about 2 V. This corresponds to region II displayed in Fig. 4(a). While the bulk photocurrent ceases, see the inset of Fig. 3(d), the edge photocurrent changes polarity, rises, and exhibits a maximum at $V_g - V_{CNP} \approx 1$ V. From the facts that in region II E_F is in the bulk gap and the photon energy is smaller than the band gap we conclude that the observed current is caused by the excitation of electrons from helical edge states into higher lying states. Different optical transitions are conceivable including those between the edge and bulk states, direct optical transitions between the spin-up and spin-down branches of the linear edge-state spectrum, and indirect transitions. Comparing the efficiencies of all the above processes [23] we attribute the circular edge photocurrents observed in the region II to the excitation of electrons from helical edge states to bulk conduction-band states (“photoionization” of the edge channels) [24, 25].

The generation of circular photocurrents via the edge-to-bulk excitation is schematically shown in Fig. 4(a). It involves similar physical concepts as used for describing photocurrents due to inter-subband transitions in semiconductor QWs [26]. Vertical arrows in Fig. 4 represent the photoionization of helical states, i.e., the depopulation of Dirac states and population of excited bulk states. The arrows end above the conduction band bottom illustrating the transitions to bulk states with nonzero transverse wave vectors k_y . For the excitation with circularly polarized radiation, e.g., σ^+ , the probability of optical transitions from the states with $s = 1/2$ is larger than those involving the states with $s = -1/2$. This is illustrated in Fig. 4(a) by arrows of different thicknesses. The resulting imbalance of the edge-state populations leads to a net electric current J^c (horizontal solid arrow). For incident radiation of the opposite helicity σ^- , the optical

transitions from the spin-down states dominates and the photocurrent reverses its direction.

The described above selection rules for the edge-to-band optical transitions can be written as

$$\frac{g_{+1/2}(k_x) - g_{-1/2}(-k_x)}{g_{+1/2}(k_x) + g_{-1/2}(-k_x)} = KP_{circ}, \quad (1)$$

where $g_{\pm 1/2}$ are the probabilities of optical transitions from the initial state with $s = \pm 1/2$, K is the coefficient describing the rigidity of the selection rules, and P_{circ} is the radiation helicity. Our calculations show that K , determined by the band structure parameters, depends only weakly on k_x and the photon energy $\hbar\omega$. In a simple 4-subband model with inversion center, the coefficient K at $k_x = 0$ is given by $2BD/(B^2 + D^2)$, Ref. [24], where B and D are the parameters of the Bernevig-Hughes-Zhang (BHZ) Hamiltonian [2]. Note that the photoexcited carriers in the conduction band also contribute to the photocurrent but this contribution is small due to fast momentum relaxation τ_p of bulk carriers.

The edge photocurrent based on the above photoionization picture requires that the initial states of the optical transitions are occupied and the final ones are empty and that the energy conservation holds. The corresponding energetic window is given by $E_c - \hbar\omega < E_F < E_c + \hbar\omega$. In real structures, the window is broadened due to inhomogeneities of the structures. Nevertheless, the range of Fermi levels and, respectively, the range of gate voltages for which this photocurrent is efficiently generated increases with increasing the photon energy $\hbar\omega$. Exactly such a behavior is observed in experiment, see Figs. 3(b),(d) and Fig. 5(a).

Calculations within the relaxation time approximation yield the following expression for the edge photocurrent

$$j_x = -\frac{eKP_{circ}}{2\pi\hbar} \int \tau_p(\varepsilon)g_{tot}(\varepsilon)d\varepsilon, \quad (2)$$

where e is the electron charge, τ_p is the momentum relaxation time determined by backscattering processes for edge carriers, $g_{tot}(\varepsilon) = g_{+1/2} + g_{-1/2}$ is the total rate of photoionization of electrons with the energy ε by circularly polarized radiation. Here, we assume that the spin relaxation of bulk carriers is fast and, therefore, photoexcited carriers get unpolarized before they are trapped back on helical edge states. This means that the depopulation of edge states determines the photocurrent.

Figure 5 compares the calculated photocurrents with the measured ones for the photon energies $\hbar\omega = 6.7$ and 10.4 meV, magnified view of the data shown in Figure 3(b) and (d). In the calculations, displayed in Fig. 5(b), we assume that $\tau_p(\varepsilon)$ is a step-like function: $\tau_p = 20$ ps for energies in the band gap, which is estimated from the length of ballistic transport edge $\sim 7 \mu\text{m}$ in our devices and the edge state velocity $\sim 10^7$ cm/s, and $\tau_p = 0.3$ ps for energies above the conduction band

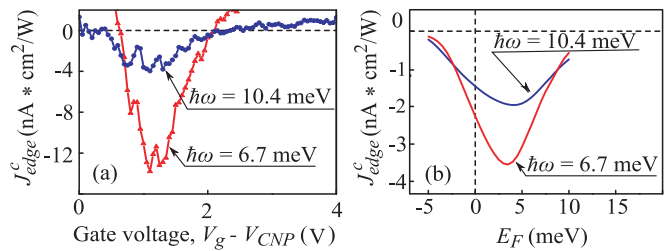


FIG. 5: (a) Circular edge photocurrents measured between the nodes of the gate dependencies. (b) Calculated edge photocurrents as a function of the Fermi level position E_F counted from the Dirac point.

bottom, which is estimated from the bulk mobility. It is seen that with a decrease of the radiation frequency the photocurrent peak narrows. Figure 5(b) shows that the theory describes the dependence of the photocurrent on the gate voltage and the radiation frequency quite well. Moreover, the calculated magnitude of the current is close to the experimental values.

Finally, we discuss region III. This region corresponds to negative gate voltages where E_F is shifted towards the valence band which in 8-nm-wide QWs has a quite complex structure. Similarly to region II, we attribute the observed photocurrent, which has the opposite sign, to optical transitions from the valence-band states to the helical edge states, see Fig. 4(b). This mechanism of photocurrent formation is essentially the same as in region II. The only difference is that the initial states are now in the valence band and the final ones are edge states. The question, though, is why the photocurrent direction reverses. To describe the current direction for a given helicity correctly one needs to assume that the selection rules for optical transitions are reversed, i.e., the transitions to the $s = +1/2$ edge states occur now dominantly for right-handed circularly polarized radiation. This, however, is at odds with the simple BHZ model Hamiltonian. In fact, this is not surprising. The valence-band structure of 8-nm-wide HgTe QWs is known to be strongly affected by the closely lying excited $|H2\rangle$ subband not included in the BHZ model, which results in a non-monotonic dispersion of the hole states and the formation of side maxima [27]. The current reversal may be also related to a strong energy dependence of the momentum relaxation time. A calculation of the optical transitions and the photocurrent requires the detailed knowledge of the real band structure and optical transitions beyond the BHZ model and will be done elsewhere.

To summarize, our results demonstrate that excitation of HgTe-based 2D TIs by circularly polarized THz radiation results in a spin polarized dc electric current flowing in helical edge channels. This observation provides a novel access for probing spin transport in TIs.

We thank G.V. Budkin for helpful discussions. The support by the DFG (SPP 1666), Elite Network of

Bavaria (K-NW-2013-247), and the Volkswagen Stiftung Program, and the RFBR (projects 15-02-06344, 16-02-01037, 16-12-10041, 16-32-00540, and 16-32-60175) is gratefully acknowledged.

-
- [1] C. L. Kane and E. J. Mele, *Phys. Rev. Lett.* **95**, 226801 (2005).
- [2] B. A. Bernevig, T. L. Hughes, and S. C. Zhang, *Science* **314**, 1757 (2006).
- [3] M. Z. Hasan and C. L. Kane, *Rev. Mod. Phys.* **82**, 3045 (2010).
- [4] X.-L. Qi and S.-C. Zhang, *Rev. Mod. Phys.* **83**, 1057 (2011).
- [5] M. König, S. Wiedmann, C. Brüne, A. Roth, H. Buhmann, L. W. Molenkamp, X.-L. Qi, and S.-C. Zhang, *Science* **318**, 766 (2007).
- [6] A. Roth, C. Brüne, H. Buhmann, L. W. Molenkamp, J. Maciejko, X.-L. Qi, and S.-C. Zhang, *Science* **325**, 294 (2009).
- [7] G. M. Gusev, Z. D. Kvon, O. A. Shegai, N. N. Mikhailov, S. A. Dvoretzky, and J. C. Portal, *Phys. Rev. B* **84**, 121302(R) (2011).
- [8] K. C. Nowack, E. M. Spanton, M. Baenninger, M. König, J. R. Kirtley, B. Kalisky, C. Ames, P. Leubner, C. Brüne, H. Buhmann, L. W. Molenkamp, D. Goldhaber-Gordon, and K. A. Moler, *Nat. Mater.* **12**, 787 (2013).
- [9] M. König, M. Baenninger, A. G. F. Garcia, N. Harjee, B. L. Pruitt, C. Ames, P. Leubner, C. Brüne, H. Buhmann, L. W. Molenkamp, and D. Goldhaber-Gordon, *Phys. Rev. X* **3**, 21003 (2013).
- [10] E. Y. Ma, M. R. Calvo, J. Wang, B. Lian, M. Mühlbauer, C. Brüne, Y.-T. Cui, K. Lai, W. Kundhikanjana, Y. Yang, M. Baenninger, M. König, C. Ames, H. Buhmann, P. Leubner, L. W. Molenkamp, S.-C. Zhang, D. Goldhaber-Gordon, M. A. Kelly, and Z.-X. Shen, *Nat. Commun.* **6**, 7252 (2015).
- [11] S. Hart, H. Ren, T. Wagner, P. Leubner, M. Mühlbauer, C. Brüne, H. Buhmann, L. W. Molenkamp, and A. Yacoby, *Nat. Phys.* **10**, 638 (2014).
- [12] C. Brüne, A. Roth, H. Buhmann, E. M. Hankiewicz, L. W. Molenkamp, J. Maciejko, X.-L. Qi, and S.-C. Zhang, *Nat. Phys.* **8**, 486 (2012).
- [13] A. Kononov, S. V. Egorov, Z. D. Kvon, N. N. Mikhailov, S. A. Dvoretzky, and E. V. Deviatov, *JETP Lett.* **101**, 814 (2015).
- [14] Z. D. Kvon, S. N. Danilov, N. N. Mikhailov, S. A. Dvoretzky, and S. D. Ganichev, *Physica E* **40**, 1885 (2008).
- [15] S. Dvoretzky, N. Mikhailov, Y. Sidorov, V. Shvets, S. Danilov, B. Wittman, and S. Ganichev, *J. Electron. Mat.* **39**, 918 (2010).
- [16] S. D. Ganichev, S. A. Tarasenko, V. V. Bel'kov, P. Olbrich, W. Eder, D. R. Yakovlev, V. Kolkovsky, W. Zaleszczyk, G. Karczewski, T. Wojtowicz, and D. Weiss, *Phys. Rev. Lett.* **102**, 156602 (2009).
- [17] C. Drexler, S. A. Tarasenko, P. Olbrich, J. Karch, M. Hirmer, F. Müller, M. Gmitra, J. Fabian, R. Yakimova, S. Lara-Avila, S. Kubatkin, and S. D. Ganichev, *Nat. Nanotechn.* **8**, 104 (2013).
- [18] E. Ziemann, S. D. Ganichev, I. N. Yassievich, V. I. Perel, and W. Prettl, *J. Appl. Phys.* **87**, 3843 (2000).
- [19] J. Karch, C. Drexler, P. Olbrich, M. Fehrenbacher, M. Hirmer, M. M. Glazov, S. A. Tarasenko, E. L. Ivchenko, B. Birkner, J. Eroms, D. Weiss, R. Yakimova, S. Lara-Avila, S. Kubatkin, M. Ostler, T. Seyller, and S. D. Ganichev, *Phys. Rev. Lett.* **107**, 276601 (2011).
- [20] M. M. Glazov and S. D. Ganichev, *Phys. Reports* **535**, 101 (2014) (2014).
- [21] M. V. Durnev and S. A. Tarasenko, *Phys. Rev. B* **93**, 075434 (2016).
- [22] S. A. Tarasenko, M. V. Durnev, M. O. Nestoklon, E. L. Ivchenko, J.-W. Luo, and A. Zunger, *Phys. Rev. B* **91**, 081302(R) (2015).
- [23] Direct optical transitions between the spin-up and spin-down branches have a low probability. Moreover, such a contribution would have a maximum for the Fermi energy lying at the Dirac point and would vanish for large negative or positive bias voltages, which is not the case. Photocurrents caused by the Drude-like free-carrier absorption require additional scattering and \mathbf{k} -dependent velocity and, therefore, seem to be weak. It can, however, provide a contribution if one takes the energy dependence of the back scattering time into account.
- [24] V. Kaladzhyan, P. P. Aseev, and S. N. Artemenko, *Phys. Rev. B* **92**, 155424 (2015).
- [25] L. I. Magarill and M. V. Entin, *JETP Lett.* **104** (2016).
- [26] S. D. Ganichev, V. V. Bel'kov, Petra Schneider, E. L. Ivchenko, S. A. Tarasenko, D. Schuh, W. Wegscheider, D. Weiss, and W. Prettl, *Phys. Rev. B* **68**, 035319 (2003).
- [27] G. M. Minkov, A. V. Germanenko, O. E. Rut, A. A. Sherstobitov, M. O. Nestoklon, S. A. Dvoretzky, and N. N. Mikhailov, *Phys. Rev. B* **93**, 155304 (2016).